Design and Integration of the EU-DEMO Water-Cooled Lead Lithium Breeding Blanket

energies

MDPI

Article

Design and Integration of the EU-DEMO Water-Cooled Lead Lithium Breeding Blanket

Pietro Arena [1,*], Gaetano Bongiovì [2], Ilenia Catanzaro [2], Cristiano Ciurluini [3], Aldo Collaku [4], Alessandro Del Nevo [1], Pietro Alessandro Di Maio [2], Matteo D'Onorio [3], Fabio Giannetti [3], Vito Imbriani [5], Pietro Maccari [1], Lorenzo Melchiorri [3], Fabio Moro [6], Rocco Mozzillo [7], Simone Noce [8], Laura Savoldi [4], Simone Siriano [3], Alessandro Tassone [3] and Marco Utili [1]

1 ENEA, Department of Fusion and Nuclear Safety Technology, C.R. Brasimone, 40032 Camugnano, Italy
2 Department of Engineering, University of Palermo, Viale delle Scienze, Edificio 6, 90128 Palermo, Italy
3 DIAEE Department, Sapienza University of Rome, 00186 Rome, Italy
4 MAHTEP Group, Department of Energy "Galileo Ferraris", Politecnico of Turin, 10129 Turin, Italy
5 CREATE, Department of Industrial Engineering, University of Naples Federico II, 80125 Naples, Italy
6 ENEA, Department of Fusion and Nuclear Safety Technology, C.R. Frascati, 00044 Frascati, Italy
7 CREATE, Engineering School, Basilicata University, 85100 Potenza, Italy
8 Industrial Engineering Department, University of Rome Tor Vergata, 00133 Rome, Italy
* Correspondence: pietro.arena@enea.it

Abstract: The water-cooled lead lithium breeding blanket (WCLL BB) is one of two BB candidate concepts to be chosen as the driver blanket of the EU-DEMO fusion reactor. Research activities carried out in the past decade, under the umbrella of the EUROfusion consortium, have allowed a quite advanced reactor architecture to be achieved. Moreover, significant efforts have been made in order to develop the WCLL BB pre-conceptual design following a holistic approach, identifying interfaces between components and systems while respecting a system engineering approach. This paper reports a description of the current WCLL BB architecture, focusing on the latest modifications in the BB reference layout aimed at evolving the design from its pre-conceptual version into a robust conceptual layout. In particular, the main rationale behind design choices and the BB's overall performances are highlighted. The present paper also gives an overview of the integration between the BB and the different in-vessel systems interacting with it. In particular, interfaces with the tritium extraction and removal (TER) system and the primary heat transfer system (PHTS) are described. Attention is also paid to auxiliary systems devoted to heat the plasma, such as electron cyclotron heating (ECH). Indeed, the integration of this system in the BB will strongly impact the segment design since it envisages the introduction of significant cut-outs in the BB layout. A preliminary CAD model of the central outboard blanket (COB) segment housing the ECH cut-out has been set up and is reported in this paper. The chosen modeling strategy, adopted loads and boundary conditions, as well as obtained results, are reported in the paper and critically discussed.

Keywords: DEMO; WCLL; breeding blanket; integration

Citation: Arena, P.; Bongiovì, G.; Catanzaro, I.; Ciurluini, C.; Collaku, A.; Del Nevo, A.; Di Maio, P.A.; D'Onorio, M.; Giannetti, F.; Imbriani, V.; et al. Design and Integration of the EU-DEMO Water-Cooled Lead Lithium Breeding Blanket. *Energies* **2023**, *16*, 2069. https://doi.org/10.3390/en16042069

Academic Editor: Guglielmo Lomonaco

Received: 9 January 2023
Revised: 7 February 2023
Accepted: 10 February 2023
Published: 20 February 2023

1. Introduction

In the roadmap to the realization of fusion energy [1], a central role is played by the breeding blanket (BB), a key component involved in at least three out of eight missions present in the roadmap itself. Indeed, tritium self-sufficiency, handling high heat fluxes to shield key components and recovering the thermal energy produced by fusion reactions are the three main duties of the BB. In order to reach this goal, since 2014, a significant effort has been undertaken towards the design of this system, with the achievement of a BB pre-conceptual design (PCD) at the end of the Framework Programme 8 (FP8) or Horizon 2020 Programme [2].

Among the different BB concepts assessed during the PCD phase, the water-cooled lead lithium (WCLL) and the helium-cooled pebble bed (HCPB) are the two BB concepts that have been selected for further studies in the conceptual design phase. The final goal is to select one of them as the "driver" blanket of the DEMO plant [2].

Both BB concepts share a considerable number of features, such as the interfaces with the vacuum vessel (VV), the remote maintenance (RM) system and the structural material, which is the reduced activation ferritic martensitic (RAFM) steel EUROFER. On the other hand, they significantly differ on the coolant, breeder and neutron multiplier materials.

The WCLL BB [3] adopts water at high pressure (15.5 MPa) and high temperature (295–328 °C) as a coolant medium, while the role of the PbLi eutectic liquid metal alloy is to multiply neutrons (Pb) and breed tritium (Li). To this end, the lithium present in the WCLL is enriched at 90% in ^{6}Li. Moreover, PbLi flowing through the blanket also plays the role of tritium carrier towards the Tritium Extraction and Removal (TER) system placed outside the VV and the bioshield.

Although the WCLL BB design has reached a quite advanced and consolidated stage, some issues remain to be solved. Indeed, a critical analysis of the work completed during FP8 was carried out by a panel of external experts [2], which identified a list of risks to be faced and mitigated. Among them, those concerning the low BB reliability and neutronic performance (low tritium breeding ratio—TBR), as well as those relevant to the coolant distribution should be mitigated by improving the design.

A general description of the WCLL BB architecture and its main neutronic, thermal–hydraulic, MHD and thermo-mechanical performances are reported in this paper, as well as some studies relevant to the BB integration in the VV.

2. WCLL BB Layout and Performances

The architecture of the WCLL BB has not significantly changed in the past few years [2–4], maintaining some cornerstones such as the adoption of the single module segment approach, two independent cooling circuits for the first wall (FW) and breeding zone (BZ), as well as the double-walled tubes (DWTs) for the cooling of the BZ.

A generic segment is composed of a C-shaped FW cooled by means of square channels and coated with a 2 mm tungsten armor, a complex of plates to stiffen the BZ (stiffening plates—SP), a system of manifolds for water and PbLi distribution and a back-supporting structure (BSS) to mainly sustain dead and electro-magnetic (EM) loads to which the blanket is subjected (Figure 1). Bundles of DWTs are in charge of removing the heat power deposited in the BZ. The internal structure of a WCLL BB segment may be thought of as the repetition in the poloidal direction of similar elementary units, also known as "slices". Concerning the manifold system, it can be divided into three main blocks. The first regards the PbLi manifold, positioned just behind the BZ and constituted by an alternance of rectangular ducts. They represent the PbLi inlet and outlet manifolds, feeding and collecting the liquid breeder to the different elementary units. The second, located just behind the former, is the BZ water manifold. It is constituted by an inlet manifold (IM) at the center of the slice feeding the 14 external DWTs, two recirculation manifolds (REC) located near the side walls collecting the water of external DWTs and feeding the eight central ones, and two outlet manifolds (OM) routing water to the outlet pipe. Finally, there are the FW manifolds, located next to the side walls and constituted by rectangular ducts developing themselves through the whole poloidal length of the segment. An overall view is depicted in Figure 2. A more detailed description of a generic WCLL BB segment can be found in [3].

Although a quite advanced design has been reached, in order to cope with temperature limitations (e.g., the suggestion to not exceed 550 °C in EUROFER components), it was necessary to modify the DWT and FW layout in some regions of the BB segment [5]. This was mainly due to the non-uniform distribution of both the FW heat flux coming from the plasma [6] and the volumetric nuclear heating due the interactions between neutrons and both structural and breeding materials [7]. The twofold outcome of this modification was

the increase in the number of FW channels per slice in the lower region of the Outboard Blanket (OB) segments from four to six, and the increase in DWT number from 22 [8] to 24 in the central part of the outboard blanket. A similar work was carried out for the inboard blanket (IB). The drawback of this change in the layout is the increase in water content in the WCLL BB, which may have a negative impact on the TBR.

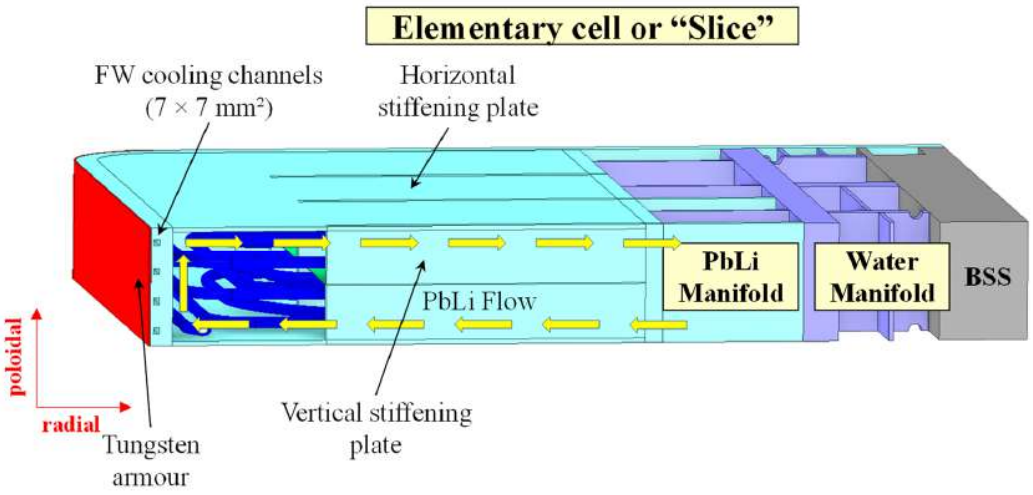

Figure 1. View of the WCLL BB elementary cell layout.

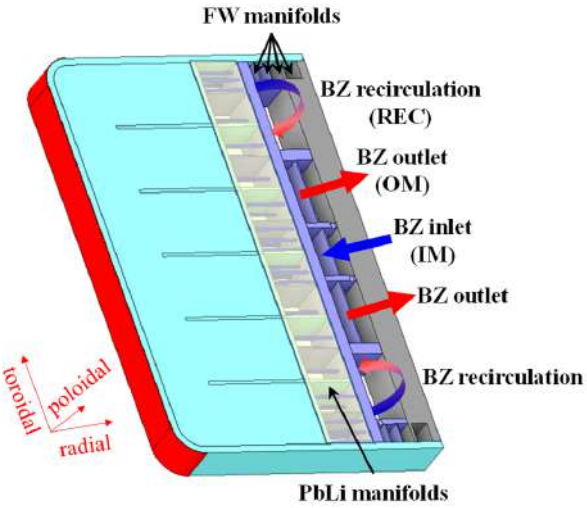

Figure 2. WCLL BB manifold scheme.

2.1. Neutronic Performances

The neutronic analyses of the WCLL breeding blanket are aimed at the evaluation of the nuclear performances of the blanket's present design, both in terms of tritium self-sufficiency and shielding capabilities, providing guidelines for further optimization of the breeding blanket structure and its future development. Three-dimensional coupled neutron and gamma transport simulations have been performed according to the guidelines on neutronic studies [9,10] by means of the MCNP5v1.6 Monte Carlo code [11] complemented with the Joint Evaluated Fusion File JEFF 3.3 nuclear data libraries [12]. The analyses have been performed using a fully heterogeneous MCNP model of the BB/manifold system developed on the basis of the DEMO 1 2017 MCNP reference configuration, representing a 11.25° toroidal sector of the tokamak [13], provided with reflective boundary surfaces on the planes that delimit the geometry, in order to simulate the whole 360° tokamak extension. The plasma parameters that define the neutron source enclosed in the model (1998 MW fusion power, neutron yield: $7.095 \cdot 10^{20}$ n/s) are shown in Table 1.

Table 1. Main parameters of DEMO baseline configuration.

Parameter	Value
N° of toroidal field coils	16
Major radius (m)	8.938
Minor radius (m)	2.883
Aspect ratio	3.1
Plasma elongation	1.65
Plasma triangularity	0.33
Fusion power	1998
Average neutron wall loading (MW/m^2)	1.04
Net electric power	500

The MCNP modeling approach adopted to achieve the generation of a detailed WCLL DEMO geometry relies on the same technique used in past analyses [7]. The EU DEMO 1 2017 baseline model has been segmented into sectors to host specific "universes" including the inboard/outboard main components: armor, FW and side walls with water channels, caps, breeding units (BU), BSS and manifolds. In particular, the area dedicated to the BZ, which is characterized by a complex layout for the cooling pipes, has been represented through the replication of the inboard and outboard equatorial BUs along the toroidal/poloidal direction by means of proper roto-translation matrixes applied to the original geometry.

The CAD models of the WCLL BB subcomponents have been pre-processed and simplified by means of the 3D modeling software Ansys SpaceClaim 2019 [14] in order to generate geometries suitable for neutronics analyses. Successively, the conversion into the equivalent MCNP representation of treated files has been carried out by means of the CAD-to-MCNP interface tool embedded in the SuperMC code [15]. The WCLL DEMO MCNP model is shown in Figure 3; the variation of the radial extension of the inboard/outboard modules in the poloidal direction has been handled keeping the distance between the FW and the innermost BB cooling channels fixed.

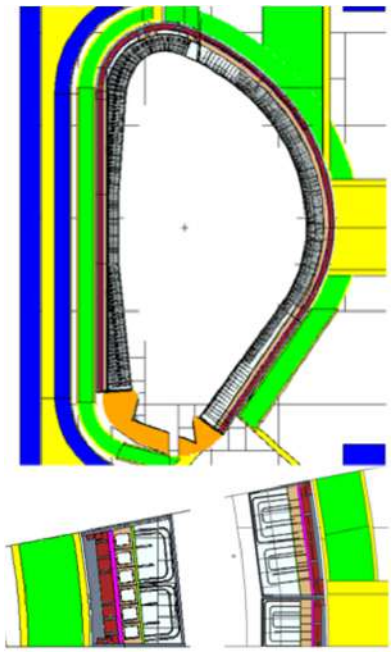

Figure 3. WCLL DEMO MCNP model: poloidal section showing the inboard and outboard breeding blanket (**top**) and toroidal section along the equatorial plane (**bottom**).

The MCNP model of the DEMO reactor integrating the WCLL BB has been employed to perform dedicated studies aimed at verifying its nuclear performances in terms of tritium generation and shielding effectiveness in protecting the toroidal field coils (TFC) of the machine. The simulations have been performed using standard MCNP cell-based (F4, F6, F1, F2 tallies) and mesh tallies (FMESH tally) with a poloidal extension that cover a single equatorial inboard and outboard BU; the tally definition is complemented with proper multipliers to calculate the needed nuclear responses.

The WCLL BB shielding performances are evaluated by means of the assessment of the neutron flux, nuclear heating density, dpa and He production in steel components along the inboard and outboard mid-plane. Figure 4 shows the inboard and outboard radial profiles of the total (in blue) and fast (E > 100 keV, in red) neutron flux from the FW up to the TFC.

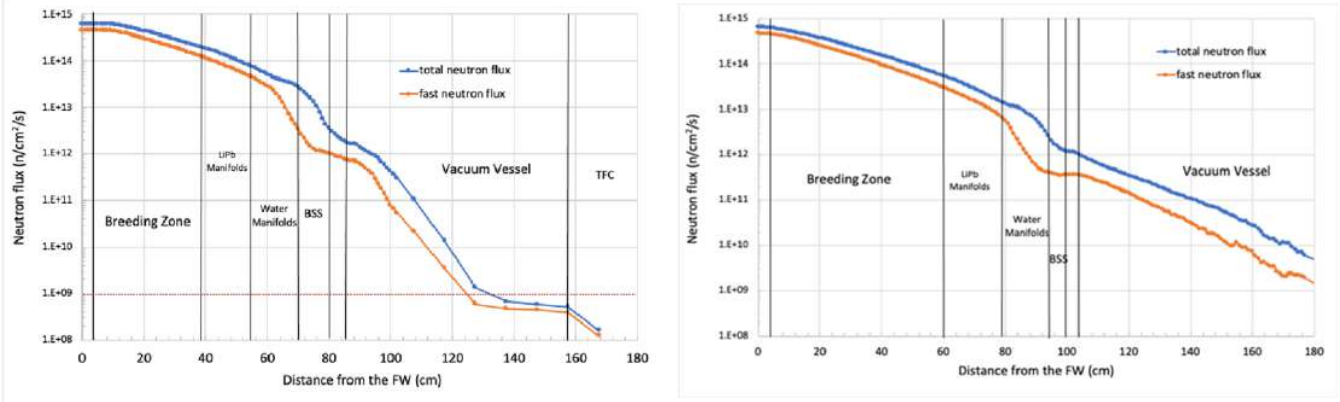

Figure 4. Total and fast neutron flux radial profiles at the equatorial plane for IB (**left panel**) and OB (**right panel**).

The total neutron flux at the inboard and outboard W armor is $6.4 \cdot 10^{14}$ n/cm^2/s and $4.65 \cdot 10^{14}$ n/cm^2/s, respectively. Inboard, the blanket/manifold system ensures a reduction of more than two orders of magnitude to the inner vacuum vessel (VV) region, and the neutron flux further decreases by three orders of magnitude across the VV, being $5.2 \cdot 10^{8}$ n/cm^2/s (total), and $3.8 \cdot 10^{8}$ n/cm^2/s (fast) on the TFC. Consequently, the WCLL BB shielding capability ensures that the 10^{9} n/cm^2/s design limit (dotted red line in Figure 4) for the fast neutron flux on the TFC is fulfilled. In the outboard sector, a three orders of magnitude attenuation of the neutron flux across the blanket/manifold system is provided. The adequate shielding performances of the WCLL BB are also confirmed by the very low values of dpa and He appm predicted within the VV. Indeed, a damage of about 0.03 dpa and helium production of 0.38 appm are predicted for the VV. Both values are well below the limits, equal to 2.75 dpa and 1 appm, respectively.

The radial profiles of the nuclear heating density evaluated in EUROFER and PbLi (BB) and SS316L (VV and TFC) for both inboard blanket (IB) and outboard blanket (OB) segments are shown in Figure 5. The highest values computed for the inboard are 23.12 W/cm^3 on the W armor and 7.5 W/cm^3 on EUROFER in the FW and 0.026 W/cm^3 on the VV inner shell SS316L. The maximum heat load density deposited onto the magnet is $4.7 \cdot 10^{-6}$ W/cm^3; thus, the BB system guarantees sufficient protection of the TFC (design limit: $5 \cdot 10^{-5}$ W/cm^3). As far as the outboard is concerned, the nuclear heating density on the W armor reaches 27 W/cm^3, while it decreases up to 9.45 W/cm^3 and $3.2 \cdot 10^{-2}$ W/cm^3, respectively, on the FW EUROFER and SS316L VV inner shell.

The assessment of the total tritium breeding ratio (TBR) aimed at the verification of the tritium self-sufficiency for the WCLL DEMO reactor has been carried out for each subcomponent of the BB that contributes to the tritium generation (i.e., breeding zones enclosed in BU and PbLi manifolds), considering the contribution due to neutron capture reactions occurring on ^{6}Li and ^{7}Li isotopes. The obtained total TBR for the present WCLL

DEMO design is 1.14, a value slightly lower than the design target for tritium self-sufficiency (1.15 [16]). With respect to the 2020 WCLL BB layout [7], the amount of water in both the inboard and outboard segments of the BB is increased, resulting in a reduced effective volume for the breeder. Moreover, the present concept also presents a slight increase in the outboard FW water content. The water has a double effect: it moderates the neutrons, enhancing the probability that they could interact with the lithium nuclei (i.e., the neutron absorption cross-section on lithium increases with the reduction in the incident neutron energy), but it also drastically inhibits the neutron streaming in the innermost breeding blanket segments. Considering these issues, a further optimization of the BZ performance in terms of tritium generation has to be taken into account in order to achieve the required TBR design target.

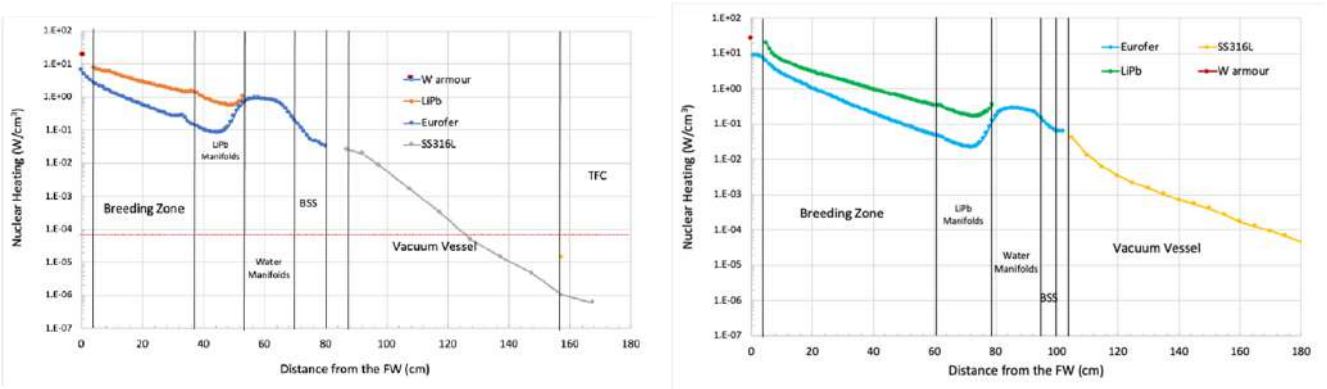

Figure 5. IB (**left panel**) and OB (**right panel**) nuclear heating radial profile in W armor, EUROFER, PbLi and SS316L.

2.2. Thermal–Hydraulic Performances

Different global and local analyses have been carried out to investigate the thermal–hydraulic behavior of the WCLL BB.

As far as the assessment of the water manifold behavior is concerned, a global analysis adopting a hybrid modeling approach was performed on the BZ one [3,17]. The DWT assembly of each half BU (11 pipes [8]) was replaced by two equivalent porous pipes (EPPs) modeled using an equivalent porous model specifically developed to mimic the hydraulic behavior of DWTs. The first pipe connects IM to the REC manifold, while the second one connects the REC to the OM. Then, the thermal–hydraulic behavior of the whole manifold was studied adopting the STAR-CCM+ code.

A steady-state thermal–hydraulic simulation has been performed, applying the neutronic nuclear heating deposited in the BZ (§2.1) to the EPP water domain. The poloidal variation in the heat generation in the different OB regions [7] has been accounted for, and the final driver in the EPP for the thermal simulation is shown in Figure 6. As far as the manifold region is concerned, the non-negligible heat generation in the EUROFER and water is directly given as a volumetric heat source to the water within the manifolds. In the simulations, the thermophysical properties of water are taken as constant in pressure and temperature, in view of the small temperature variation expected for the coolant. RANS equations are used to account for water turbulent conditions, and the k-ω SST turbulence model is used, including the Γ-transition option to allow capturing the transition to laminar flow that could occur at low values of flow rates (REC manifold, beginning of the OM and end of the IM).

The flow imbalance among the breeding units was already reported in [3]; in Figure 7a, the flow distribution along the manifolds is rather reported, showing the expected decrease and increase in the IM and OM, respectively, and a small net flow along the REC.

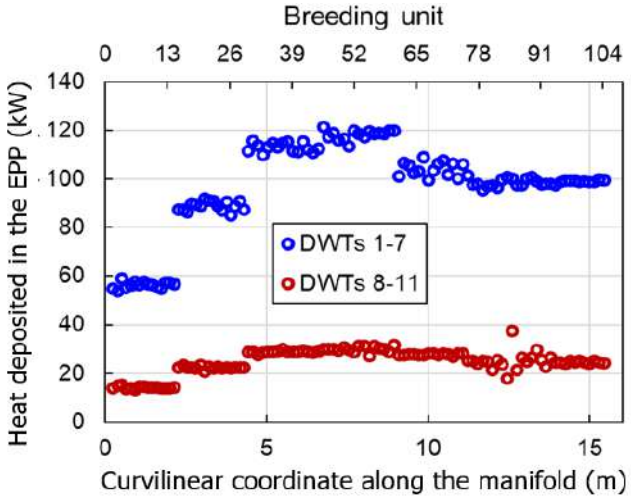

Figure 6. Heat deposited in each EPP along the curvilinear coordinate of the manifolds—*s*.

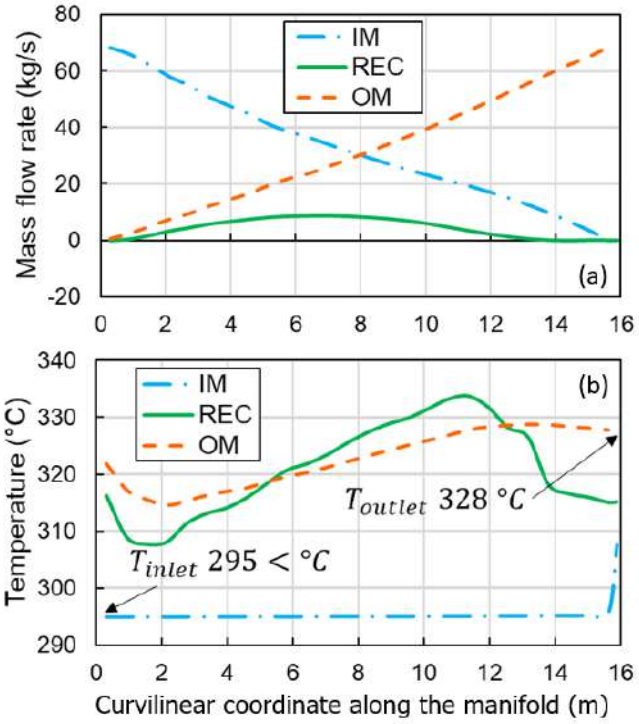

Figure 7. (**a**) Flow rate and (**b**) bulk temperature distribution along the manifolds.

The corresponding bulk temperature distribution computed along the manifolds is reported in Figure 7b. The temperature of the IM is nearly constant and equal to the inlet temperature of the water, which is 295 °C. Only in the upper centimeters of the manifold, the temperature in the IM rises by ~15 °C due to the absence of DWTs, which creates a stagnant water zone. In the OM, temperature increases almost linearly in the central part of the manifold, between s = 2 m and s = 12 m. In the bottom part, s < 2 m, the temperature of water is higher because of the low mass flow rate in OM (Figure 7a); in the upper part, s > 12 m, the mixing temperature along the OM decreases slightly, and then it exits at an outlet temperature of 328 °C. The most peculiar behavior of the temperature in the manifolds is observed in REC. Here, the temperature of water increases considerably and overcomes the OM temperature in the central part of the manifold. This effect can be explained as a combination of the heat generation inside the REC, where a poor net flow is present, and the hot water entering the REC from the EPPs is exposed to high heating

(Figure 6). Overall, it is anticipated that the bulk fluid temperature remains everywhere below 335 °C. Note that this kind of hybrid model is not suited to localize hot spots at the wall since no conjugate heat transfer problem is solved.

The imbalance of the mass flow rate distribution and consequently of the temperature one, suggest that orifices or layout modifications are necessary for the manifold system to allow a correct mass flow distribution and cooling capability.

In addition to results on the BZ manifold behavior, neutronic results also highlighted the necessity of a WCLL BB revision to enhance the TBR. To this end, a new DWT layout has been investigated. It consists of six couples of helical-shaped DWTs, each one positioned between two vertical stiffening plates or between the side wall and a vertical stiffening plate (Figure 8). The rationale behind this design is a reduction in water in the BZ region (more TBR), a better cooling capacity and a simpler flow distribution (no recirculation). As in the C-shaped configuration, all the tubes have an internal diameter of 8 mm and an external diameter of 13.5 mm.

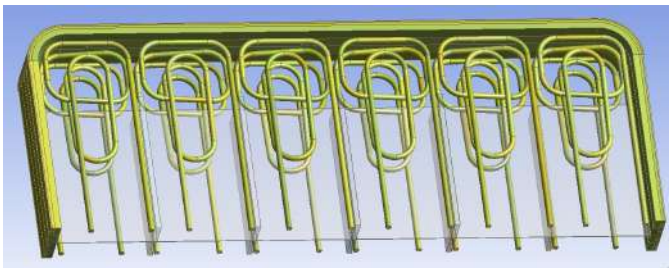

Figure 8. Helical-shaped DWT layout in the COB segment.

Each couple of tubes consists of two slightly different DWTs. DWT-1 (on the left in Figure 9) includes a pair of straight inlet–outlet pipes of the same length extending in the radial direction. The helicoidal part of the pipe, positioned closer to the FW, is made of 10 bends and 9 straight sections, for a total of 2.5 windings. The tube is designed such that part of the first and last windings are located on the same radial–toroidal plane (i.e., horizontal). This is to maximize the DWT surface closer to the radial–toroidal stiffening plates to be uniformly cooled. Concerning DWT-2 (on the right in Figure 9), it is composed by straight radial inlet–outlet pipes of the same length and a helicoidal part made of 10 bends and 4 straight sections, for a total of 2.5 windings.

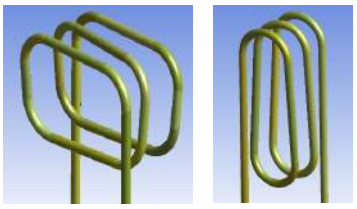

Figure 9. DWT-1 (**left**) and DWT-2 (**right**) layout.

Each couple of DWTs is located in a slot of the segment such that the tubes are equidistant between two consecutive radial–poloidal and radial–toroidal stiffening plates. The distance of the DTWs from the FW has been optimized with CFD calculation with the aim of reducing the hotspots. The main characteristic data concerning helicoidal DWTs are reported in Table 2.

In order to evaluate the effectiveness of this DWT layout, a CFD simulation of an equatorial slice of the COB segment equipped with the helical-shaped DWTs was carried out. The Ansys-CFX code was used and the k-ω Shear Stress Transport turbulence model was adopted. A fine mesh was created by imposing a value of $y^+ = 1$ to the inflation control near the walls for the resolution of the viscous sub-layer in all the fluid domains

(i.e., water flowing into FW channels and DWTs). A steady-state calculation reproducing the plasma flat-top conditions was performed. A heat flux value of 0.32 MW/m^2 was imposed onto the FW plasma-facing surface [6], while the nuclear heating calculated in [7] was considered for water, EUROFER and PbLi. A water inlet temperature of 295 °C was considered. The total mass flow rate flowing within DWTs was adjusted to obtain an average output temperature of 328 °C. As in previous studies [8,18], the PbLi breeder was conservatively treated as a solid, neglecting buoyancy and mixing phenomena that could enhance the cooling capability of the BZ.

Table 2. Helical-shaped DWTs characteristics.

Parameter	DWT 1	DWT 2
N° of tubes in COB elementary cell	6	
Number of windings	2.5	
Distance from FW	10.0 mm	46.0 mm
Total length (in BZ)	2506.1 mm	2353.6 mm
Toroidal dimension	226.5 mm	106.5 mm
Poloidal dimension	120.0 mm	117.5 mm
Radial inlet–outlet part	476.7 mm	440.7 mm
Curvature radius	46.5 mm	
Helix inclination	4.95°	

Results obtained from the CFD calculation (Table 3) show that despite the high thermal loads, the helical-shaped DWTs layout is guaranteed to keep the EUROFER temperature below the limit of 550 °C. Indeed, the maximum EUROFER temperature is equal to 545.1 °C and it is reached on a radial–toroidal stiffening plate, as shown in Figure 10. The main results obtained from the calculation are given in Table 3.

Table 3. Main results with the new DWT layout.

Parameter	Value	Unit
FW water total mass flow rate	0.63	kg/s
BZ water total mass flow rate	0.21	kg/s
DWTs average outlet T	327.5	°C
FW average outlet T	328.7	°C
Max T in Plates	545.1	°C
Max T in FW	529.5	°C
Max T in Pb-Li	618.3	°C
Pressure drops in DWT-1	0.260	bar
Pressure drops in DWT-2	0.147	bar

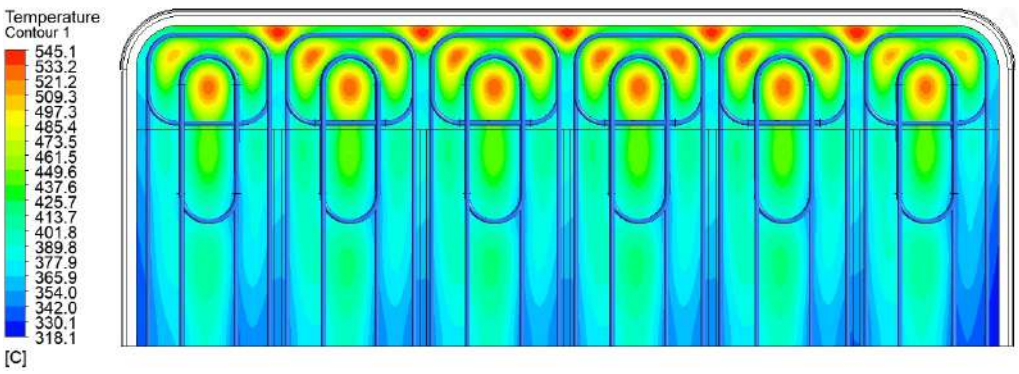

Figure 10. Temperature field on radial-toroidal stiffening plate.

2.3. MHD Performances

A fork of RELAP5/mod3.3 (R5-MHD), a system thermal–hydraulic code, has been developed to make possible a quick and reliable estimate of MHD pressure loss in the WCLL BB and the PbLi loop [19,20]. To demonstrate its capability, R5-MHD was used in a test case based on the WCLL test blanket module (TBM) geometry, where it demonstrated adequate qualitative and quantitative accuracy compared with pressure drop estimates made with direct numerical simulations [21]. Given its acceptable performances, R5-MHD was applied to the simulation of the WCLL BB loop to update the total MHD pressure drop estimate performed in 2018 and 2019 using semi-analytical methods [22,23].

The R5-MHD model is consistent with that described in [19,21]: all the system components are nodalized with 1D elements and a slice technique is adopted to ensure consistency in the definition of mesh height and hydrostatic pressure. The WCLL PbLi loop in R5-MHD includes all regions with a significant magnetic field intensity (>100 mT), considering both toroidal and poloidal components [24]. The PbLi is assumed to flow isothermally at T = 600K with physical properties evaluated according to [25]. For IB and OB segments, flow rates are taken as Γ_{OB} = 16.38 kg/s and Γ_{IB} = 5.34 kg/s [22].

The pressure (minus the hydrostatic component) profile for the hydraulic path corresponding to the central channel in the equatorial cell of the OB model is shown in Figure 11, and the contribution of each hydraulic section is detailed in Table 4 for both IB and OB. The profile for IB is qualitatively similar. The connection between the manifold and the BZ is assumed to consist of 1 cm × 1 cm square windows. Total pressure loss in OB and IB is consistent with the previous estimate, from 23.5 to 25.8 bar, and confirms that a significant contribution is given by the inlet (FP) and outlet (DP) pipes that connect the BB and tritium extraction removal (TER) loop. Regarding OB, the spinal and bottom collectors are also pressure drop-intensive and are the regions where the estimate is going to benefit the most from dedicated CFD analyses.

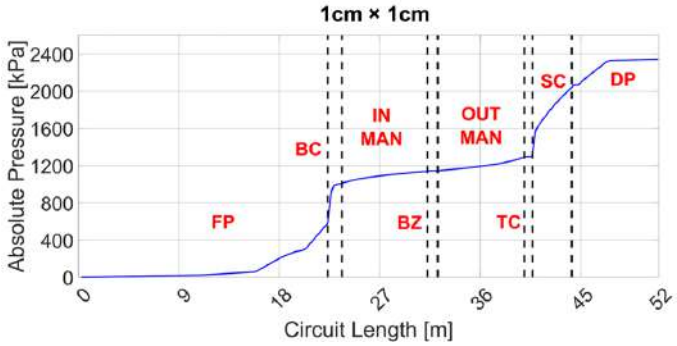

Figure 11. Pressure as a function of circuit length in OB loop. Hydraulic sections: feeding pipe (FP), bottom collector (BC), inlet manifold (IN MAN), BZ, outlet manifold (OUT MAN), top collector (TC), spinal collector (SC), outlet pipe (DP).

Table 4. Pressure drop (in kPa) in OB and IB loop broken down by hydraulic section (cf., Figure 11 caption).

Area	**OB**		**IB**	
	This study	Ref. [23]	This study	Ref. [23]
FP	581	613	1499	1557
BC	422	122	84	92
IN MAN	136	68	275	328
BZ	5	n/a	17	n/a
OUT MAN	148	190	275	122
TC	30	55	5	76
SC	718	444	null	null
DP	303	429	428	260
TOT	2343	1921	2583	2435

The flow rate distribution between the radial–poloidal cells is expected to be relatively uniform due to the electromagnetic coupling, even if a discrepancy may exist between the equatorial and terminal ones due to the manifold layout [26]. Figure 12 shows the differential pressure between OB BZ cells, which is qualitatively consistent with [26], even if coupling is currently not modeled in R5-MHD.

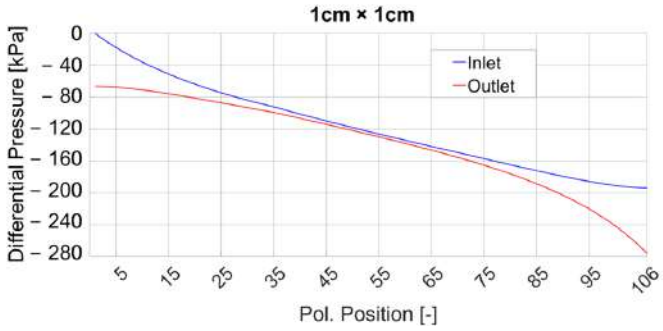

Figure 12. Differential pressure between OB inlet and outlet manifolds as a function of the discretized poloidal position (i.e., BZ cell). This quantity is directly proportional to BZ flow rate.

Flow repartition is expected to reach up to 300% of the nominal flow (0.155 kg/s) for the terminal ones and as low as 25% for the equatorial ones. These values must be intended as indicative since they are going to be affected by coupling, even if the accurate agreement in terms of overall pressure loss between our model and CFD calculations for the WCLL TBM (see Ref. [21]) suggests that, at least for this configuration, no significant pressure penalty should be expected. Regarding IB, flow repartition is even more skewed towards the terminal ones, where it reaches up to 500% of the nominal value (0.056 kg/s) and 10% for equatorial ones.

Dedicated CFD analyses have also been conducted to characterize the magnetoconvective regime in the OB equatorial elementary cell considering an idealized pipe layout (straight toroidal tubes) [27]. Compared to previous studies [28,29], the present model aimed to investigate the effect of a skewed magnetic field, more accurate FW thermal boundary conditions and higher magnetic field intensity (≈4 T, Ha = 9159).

In addition to the intense and spatially varying volumetric heating [28], a surface thermal load equal to 0.32 MW/m^2 was imposed on the external face of the tungsten layer (2 mm thick). Heat removal in the FW was simulated considering an imposed convective boundary condition on the surface of the four square colling channels rather than on the whole FW surface, which unduly magnifies the available heat sink [6,28]. The computing resources and the related technical support used for this work were provided by CRESCO/ENEAGRID High Performance Computing Infrastructure and its staff [30].

Figures 13 and 14 show the velocity and temperature distribution at Ha = 9159. In broad agreement with the previous studies [27,28], no temperature fluctuations were identified after 100–300 s of transient, and heat transfer was still dominated by conduction, with Nusselt numbers from 1.1 to 1.2. The inclined magnetic field disrupts the large-scale convection cells and promotes a more granular structure of cells, as shown in Figure 13. This phenomenological change appears to have had a minor impact on the heat transfer regime, which remained consistent with that from [28]. The maximum velocity, relative to a value of 13.5 mm/s, is located in proximity of the baffle plate, where the MHD internal layer develops. The more accurate boundary condition for the heat sink in the FW causes an increase in the predicted temperature of about 90 K with respect to the ones computed in [28], suggesting a narrower safety margin with EUROFER limit temperature compared with previous calculations. The minimum and maximum values in Figure 14 are related to 342 °C and 467 °C, respectively.

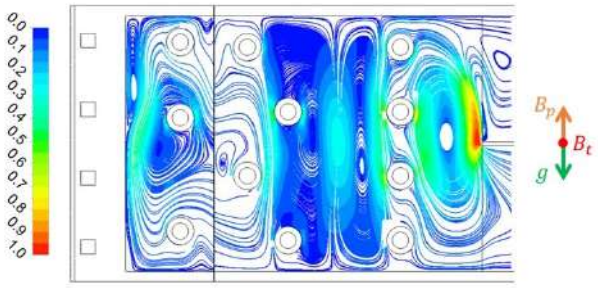

Figure 13. Dimensionless velocity streamlines (u/u_{max}) on the radial–toroidal plane in the middle of the cell.

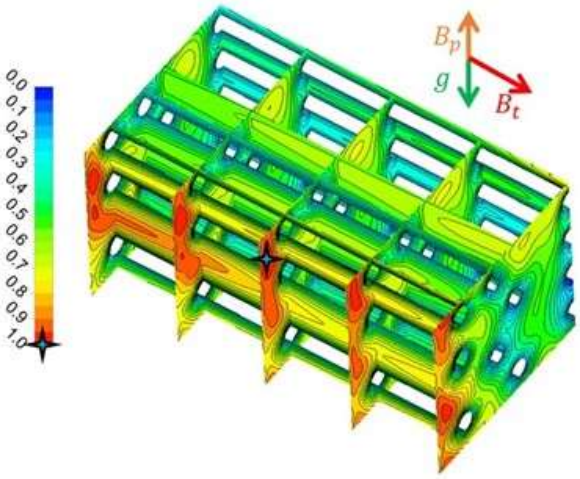

Figure 14. Scaled temperature distribution ((T–T_{min})/(T_{max}–T_{min})) in different planes.

2.4. Thermo-Mechanical Performances

With the aim of evaluating the structural performances of the WCLL COB segment, thermo-mechanical analyses under nominal and accidental loading scenarios were carried out. In addition, local analyses aimed at investigating more in detail the structural performances of some regions of interest were performed.

Thanks to a purposely set-up procedure [31], a realistic 3D thermal field was estimated and applied to the whole COB segment [5] without performing the thermal analysis of the whole segment, which would have implied a tremendous computational burden. Then, its structural behavior was evaluated under different steady-state loading scenarios in view of the RCC-MRx structural design code [32]. In particular, as reported in [5], the normal operation (NO), over-pressurization (OP) and upper vertical displacement event (UVDE) scenarios, classified in the RCC-MRx code as Level A (i.e., nominal), Level D (i.e., sever accident) and Level C (i.e., off normal condition), respectively, were considered.

The results show that the COB segment experiences, in all the assessed scenarios, a qualitatively similar displacement field, with an evident radial displacement in the equatorial region (for example, in Figure 15, displacements under NO and OP scenarios are reported), suggesting a revision of the attachment system. Moreover, a stress linearization procedure performed in some critical regions of the internal stiffening plates (SPs) allowed verifying the fulfilment of the pertinent sets of RCC-MRx rules. The results have shown that the criterion considering the secondary stresses, namely that against the immediate plastic flow localization, is largely not met especially in the equatorial region, mainly because of the excessive thermal deformation.

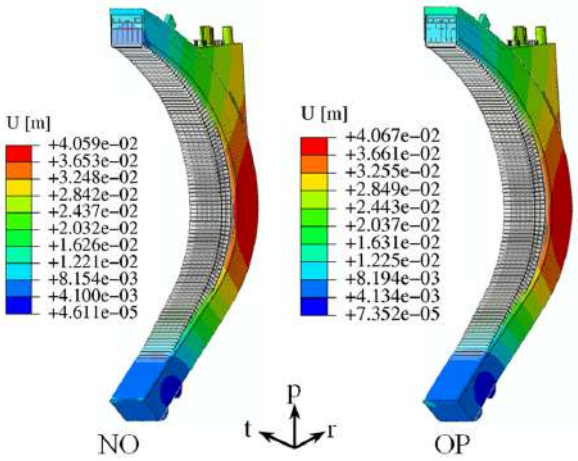

Figure 15. Deformed vs. undeformed shapes and displacement fields under NO and OP loading scenarios.

In a second phase, the sub-modeling technique was applied to locally assess in detail the structural performances of some regions of interest. Thanks to this approach, it is possible to assess the local thermo-mechanical behavior of some regions of the segment imposing, as boundary conditions, the displacement field previously calculated in the analysis of the whole segment in the considered loading scenario. Finally, applying the sub-modeling technique, it is also possible to perform detailed structural analysis of the segment box (SB), as the local model includes the cooling channels, not modeled in the whole segment analysis to save computational resources. Therefore, 3D FEM models reproducing the top (TC), central (CC) and bottom cells (BC) of the COB segment endowed with the SB cooling channels, each consisting of a triplet of elementary cells located at different poloidal heights, have been set up. Thermo-mechanical analyses under NO, OP and UVDE scenarios have been performed, considering the corresponding set of loads and boundary conditions.

The obtained results have allowed assessing in detail the stress locally arising within the considered regions. As an example, the spatial distribution of the Von Mises equivalent stress under the NO scenario is depicted in Figure 16. Here, the results obtained from sub-modeling analysis are superimposed to those obtained from the analysis of the whole segment, showing continuity in the spatial distribution, thereby demonstrating the predictive power of the sub-modeling technique.

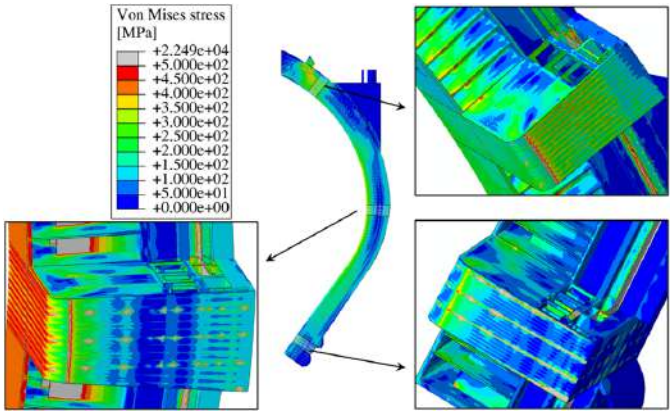

Figure 16. Von Mises stress field within top, central and bottom models in NO superimposed to the global model.

The results, in terms of fulfilment of the RCC-MRx design criteria, show that within the first wall-side wall (FW-SW) region, the equatorial part of the segment is still the most

stressed, as already obtained in the global analysis. Therefore, these outcomes again suggest a revision of the attachment system, in order to reduce the large displacements and the high stress level occurring in that region. As an example, in Figure 17, the obtained results, in terms of RCC-MRx design criteria verification, in the NO loading scenario within the FW-SW region are reported.

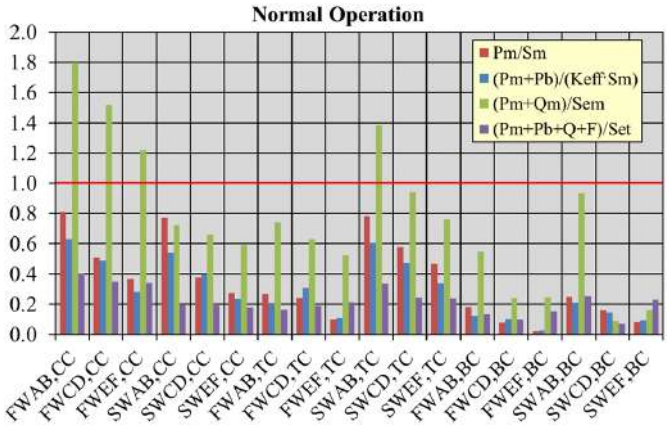

Figure 17. RCC-MRx criteria verification in NO loading scenario within FW-SW.

In addition, it can be observed that comparing the results of the RCC-MRx rules verification obtained within SPs in the global model (GM) and sub-model (SM) analyses, similar behavior can be observed. As an example, in Figure 18, the comparison in the NO loading scenario for the central sub-model is reported. Therefore, since a similar behavior is observed, this allows us to conclude that in the sub-modeling analysis, the attention and the modeling effort can be focused on the FW-SWs region since the global analysis already provides reliable results concerning the SPs domain.

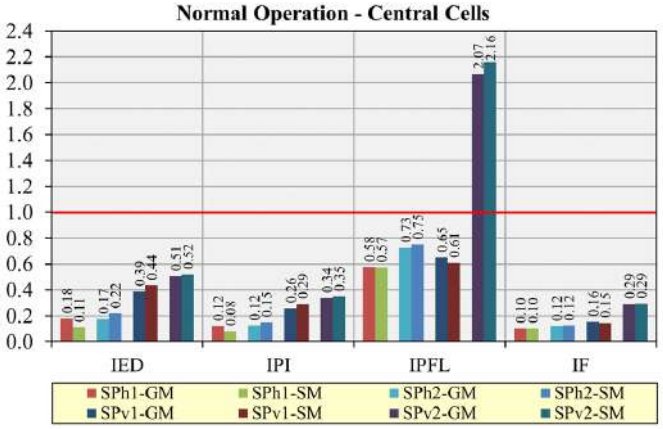

Figure 18. RCC-MRx criteria evaluation within global model and CC sub-model in NO scenario.

3. Integration

One of the main efforts carried out during the DEMO PCD phase has been the in-vessel integration of the BB with the primary heat transfer system (PHTS) and TER. A combination of requirements from RM, divertor and VV design, as well as space limitations, forced the routing of all the coolant pipes through the upper port. The unique pipes routed through the lower port are the PbLi feeding pipes.

Concerning the PbLi, an inlet and an outlet pipe per segment are foreseen. DN 200 pipes are foreseen for OB segments, while DN 125 and DN 150 pipes are envisaged as inlet and outlet tubes of IB segments, respectively. As far as the water coolant is concerned, it is distributed to FW and BZ circuits by proper feeding pipes. FW water is routed to and collected from

segments by DN 100 and DN 125 pipes for IB and OB segments, respectively. On the other hand, BZ water is delivered and re-collected from segments by means of DN 100 and DN 200 pipes for IB and OB segments, respectively. A dedicated analysis is being carried out with the aim of evaluating whether the present layout allows the draining of both water and PbLi from the segments.

Moreover, other components such as heating systems and diagnostics need to be integrated in the BB. To this end, a dedicated study on the integration of the electron cyclotron is being carried out.

3.1. Electron Cyclotron Heating Integration

The integration of the electron cyclotron heating (ECH) system in the BB will strongly impact the segment design [33]. In the current configuration, the ECH is assumed to be positioned in the equatorial port of DEMO. Starting from this assumption, a preliminary integration study has been conducted to evaluate the impact of the cut-outs needed for the cone waves on the COB segment design.

The design guidelines are represented by the cone waves of ECH that must reach the in-vessel toroidal chamber of DEMO (Figure 19).

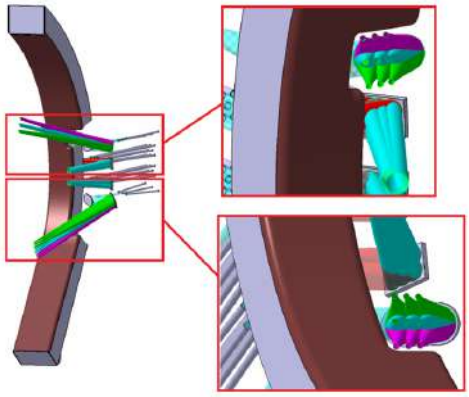

Figure 19. Path of the ECH electromagnetic waves.

Cut-outs have been introduced into the segment structure to allow for the passage of these beams. The toroidal width of the segment impacted has been reduced in the area of the ECH cone waves, and two different steps have been introduced in the segment structure (Figure 20):

- The first one extends for 500 mm from the side wall and with a poloidal length of about 4350 mm;
- The second one extends an additional 210 mm (710 in total from the side wall) with a poloidal length of about 850 mm.

The size of the cuttings has been minimized, but the internal structural layout of the BB segment has inevitably been affected. Indeed, the three main areas that compose the BB slice have been modified: the water manifold zone, the PbLi manifold zone and the BZ.

The current BZ cooling water manifold reference configuration includes one input manifold (Figure 20 yellow), two recirculation manifolds (Figure 20 blue) and two output manifolds (Figure 20 green). As a result of the first step, one of the two recirculation manifolds is trimmed, while the remaining ones are diverted and reduced. As a result of the second step, the remaining manifolds are further diverted and reduced.

Consequently, the layout of the BZ water cooling channels (DWTs) will be modified according to the new position of the water manifold. The first wall cooling water manifolds (Figure 20 pink) are simply moved along the edges of the first wall following the cut-out profile.

The current slice reference configuration foresees six lithium lead manifolds. As a result of the first step, they are reduced to four, and because of the second, they are reduced to three (Figure 21).

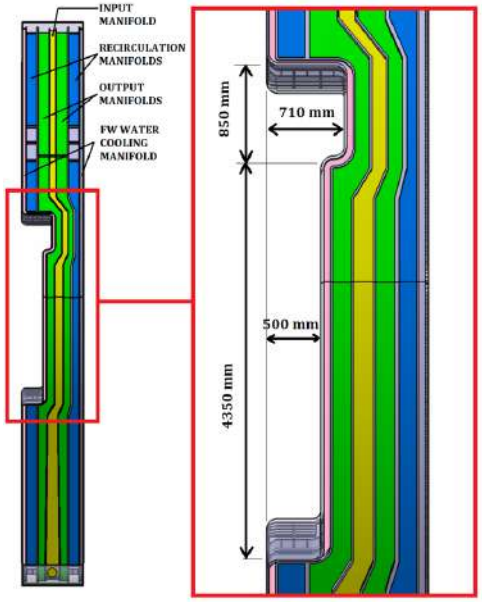

Figure 20. Cut-out of the BB COB segment—back view of the water-cooling manifold area.

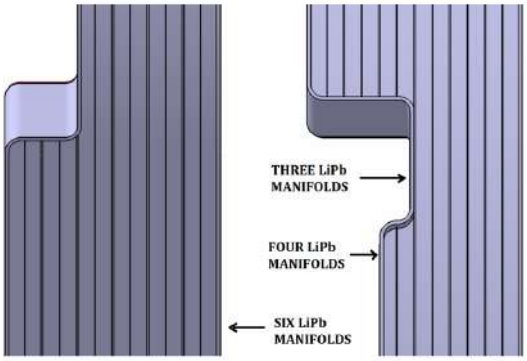

Figure 21. Back view of the COB segment with a detail of the PbLi manifold.

The holes on the backwall that allow the path of the PbLi in the poloidal direction of the BZ will also be used to allow the transfer of the PbLi from the trimmed to the untrimmed manifolds (Figure 22). Conversely, at the end of the cut-out, they will be used to feed the manifolds that recur after the narrowing.

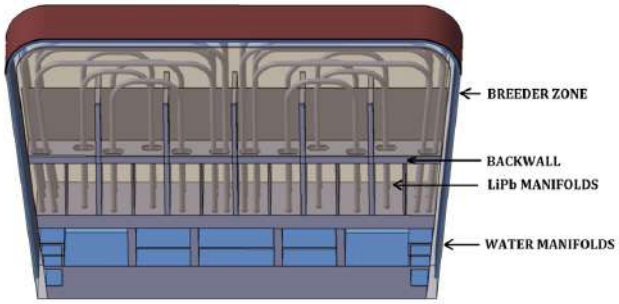

Figure 22. Detail of the backwall holes allowing the PbLi circulation.

In order to assess the integration of the WCLL BB with the ECH system from a structural point of view, a preliminary analysis of the WCLL COB segment endowed with ad hoc cut-outs was performed. To this end, the purposely developed geometric layout was equipped with the reference attachment system, devoted to connecting the segment

to the vacuum vessel. As in the reference design [3], EUROFER steel was considered as the structural material, assuming a 2 mm thick tungsten layer covering the FW. Then, a 3D mesh composed of ~2.8 M nodes connected in ~5.1 M elements was set up.

Preliminary steady-state structural analysis was performed under the normal operation (NO) and over-pressurization (OP) loading scenarios, only considering thermal, mechanical and gravity loads. The obtained results were evaluated in view of the RCC-MRx structural design code [32], adopting the pertinent set of design rules. Indeed, the NO scenario represents the nominal operative conditions of the WCLL BB, being classified as Level A in the RCC-MRx code, whereas the OP scenario is a conservative accidental scenario consisting of the pressurization of the whole segment box because of a coolant leakage, being classified as Level D.

Concerning the 3D thermal field, the reference one [5] was mapped to the considered geometric layout, as shown in Figure 23.

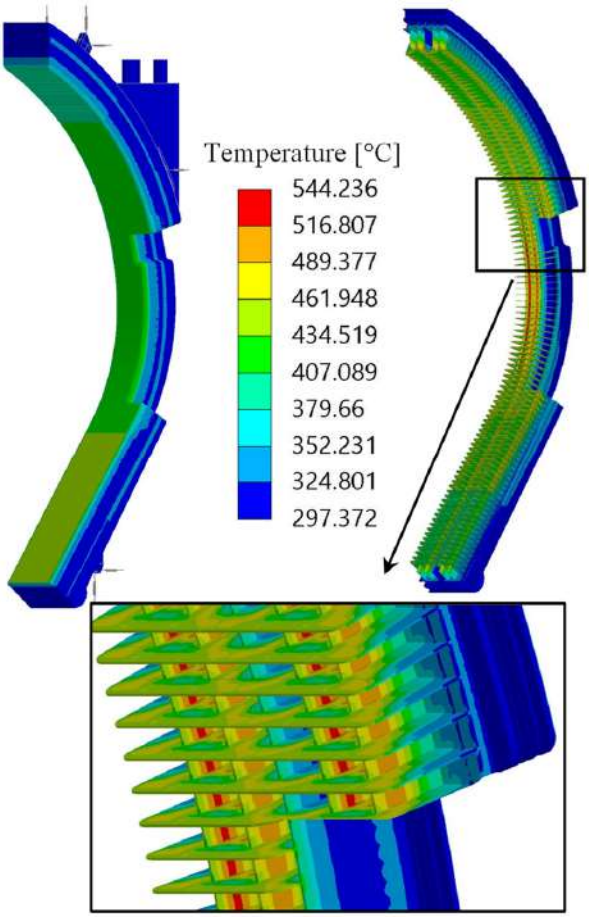

Figure 23. The imposed 3D thermal field.

Regarding pressure loads, in the NO scenario, the water and breeder design pressure of 17.825 MPa and 0.575 MPa, respectively, have been assumed, whereas in the OP scenario, the water design pressure has been imposed everywhere to assess the segment overall pressurization. Moreover, the gravity load has been imposed, applying a temperature-dependent equivalent density to the steel domain in order to take into account the masses of the breeder and the water, not directly modeled. Lastly, the attachment mechanical action has been simulated imposing proper spring elements (partially visible in Figures 23 and 24) whose equivalent stiffness values have been drawn from the reference analysis [3].

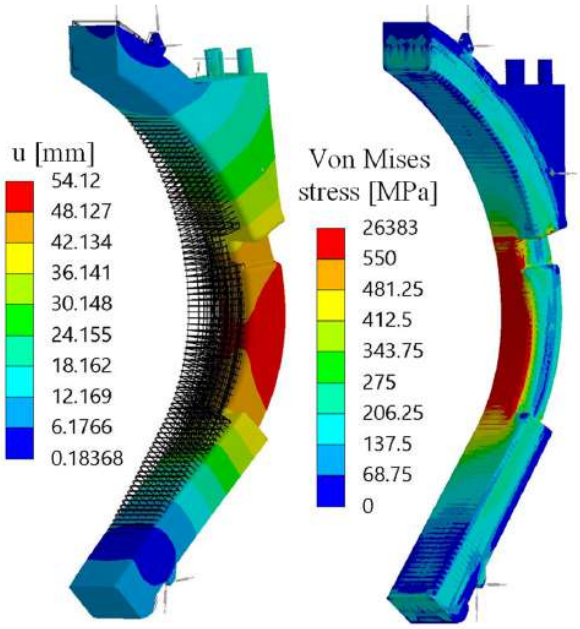

Figure 24. OP scenario—displacement (isotropically amplified by a factor 20) and Von Mises stress fields.

The results in terms of displacement field, on a deformed shape superimposed to the undeformed shape, and Von Mises equivalent stress field are depicted in Figure 24. For the sake of brevity, only results referring to the OP scenario are shown. As it can be observed, as in the reference configuration [5], the maximum displacement and stress are predicted in the equatorial region, mainly because of the attachment layout.

In the end, a stress linearization procedure was carried out along purposely selected paths, whose locations are shown in Figure 25. The fulfilment of the set of criteria relevant to Level A and Level D, for the NO and OP scenarios, respectively, was checked. The results obtained for the paths located in regions A, B and C, particularly where the cut-outs are the most invasive in the segment, are reported in Figure 26.

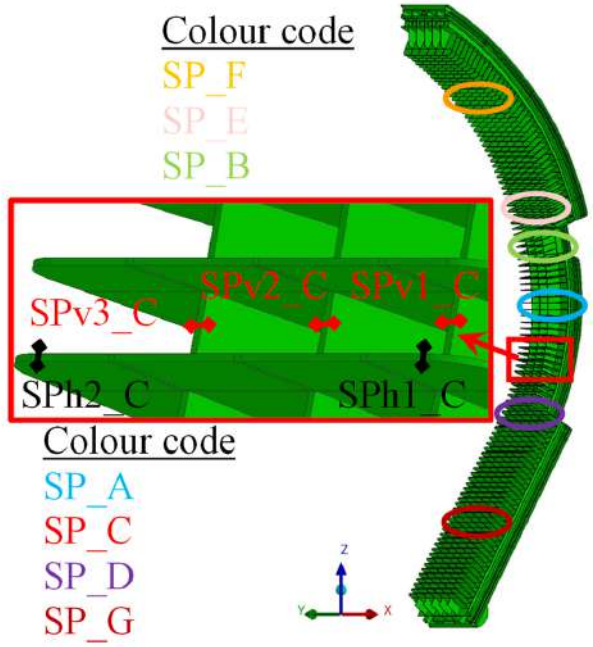

Figure 25. Locations of paths for the stress linearization.

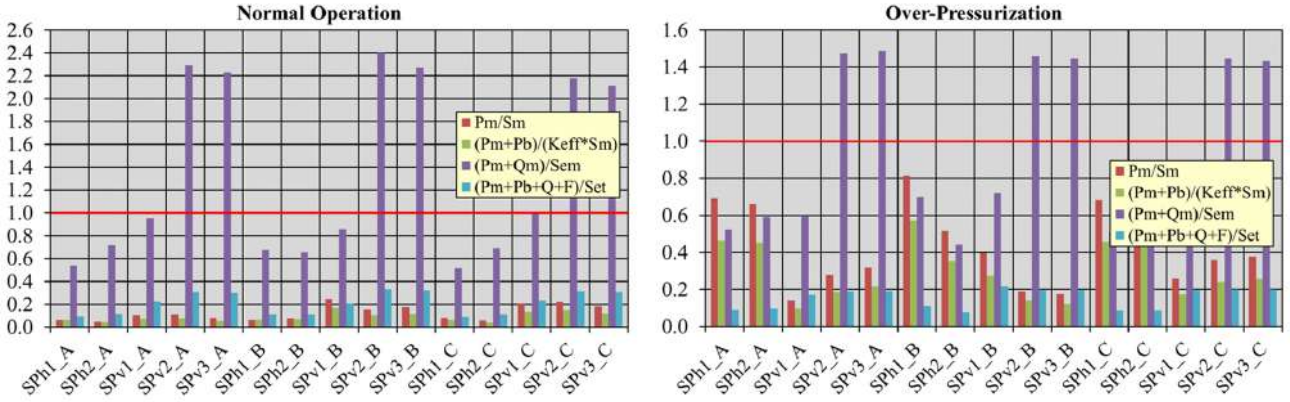

Figure 26. RCC-MRx cNO (**left**) and OP scenarios (**right**).

The results clearly show that the criterion against immediate plastic flow localization $(P + Q)_m/S_{em}$ is the most critical in both the assessed scenarios. Criteria considering only primary stress are widely satisfied in the NO scenario and satisfied with a reduced, yet acceptable, margin in the OP loading scenario.

Lastly, in Figure 27, a comparison with the results of the $(P + Q)_m/S_{em}$ criterion verification obtained in the reference WCLL COB structural analysis [5] is depicted. For the sake of brevity, only results relevant to the NO scenario are reported since the same conclusions are qualitatively obtained for OP. From the reported results, it can be observed that the introduction of the cut-outs worsens the segment structural performances in the regions A, B, C, D and E by ~40% at the most. Instead, looking at the same comparison made for regions F and G, namely the regions far enough from the cut-outs, it is possible to notice an improvement in the structural performances. This is due to the fact that, since the equatorial region of the segment is less stiff than the reference design because of the introduction of the cut-outs, the top and bottom regions can relax more at the expense of the central one. This effect derives from the attachment system layout which prevents a significant vertical expansion of the BB segments, compelling the structure to deform toward the center.

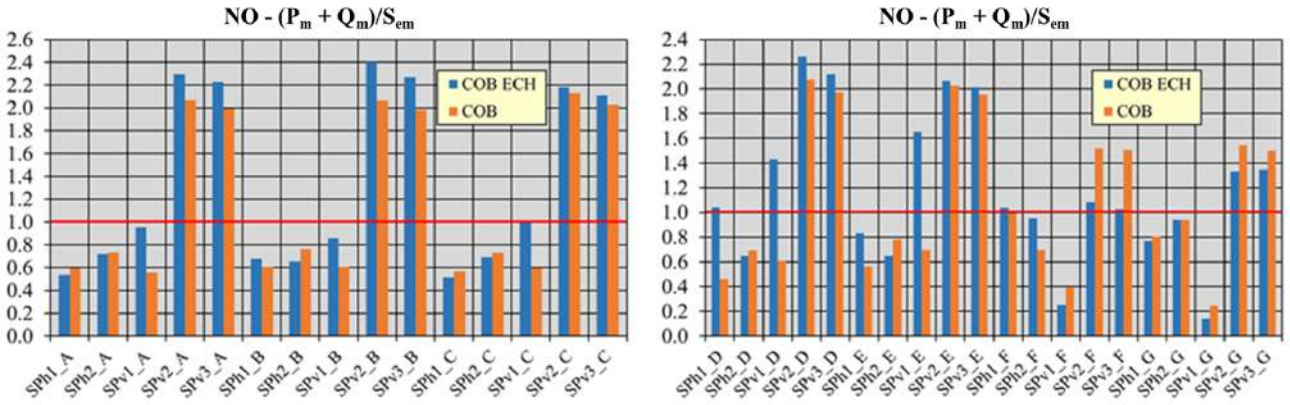

Figure 27. Comparison to the reference results.

3.2. Process Fluid Integration

A preliminary procedure to drain the water coolant from a DEMO tokamak sector was proposed and investigated using numerical tools. The focus was on the BZ system and the COB segment, but the considered assumptions may be easily extended to other sector segments and to the FW system.

3.2.1. Assumptions

Various aspects are involved in defining a draining procedure consistent with the DEMO reactor requirements and operative conditions. In this study, it is assumed that:

- Draining is executed during long-term maintenance (LTM) [34] or when a segment substitution is needed.
- Water is drained after PbLi to avoid freezing the lead lithium within the segment (occurring at ≈235 °C [25]).
- Draining transient is represented by a single BB COB segment. Since no isolation valves are foreseen on the collectors/distributors connecting the blanket sectors to the PHTS, each blanket sector cannot be drained separately from the others as well as independently from the rest of the PHTS circuit. For this activity, we focus on a single BB segment in a given sector but, ideally, one should consider the BB as a whole.
- The BB segment is drained from the top using gas injection. Either gravity, installing a correspondent pipeline at the component bottom, or gas injection can be used to accomplish the objective. The former solution introduces a potential risk source since draining pipe failure would start a severe LOCA sequence, and it is discarded. Nitrogen is assumed as the injection gas.
- BB PHTS is assumed in hot standby mode at transient start, consistently with the LTM assumption. The primary circuit is at an average temperature equal to the minimum system temperature (295 °C [35]) and zero flow.
- Component gas must be injected with enough overpressure to remove water from the blanket. The maximum gas pressure was preliminarily assumed to be equal to the BB PHTSs nominal pressure (15.5 MPa [35]), since exceeding this parameter during an operational procedure was considered not advisable for the system. The water loop must be depressurized to ensure a sufficient differential pressure between gas and water. The BB pressurizers can be used for this purpose. After disabling their nominal pressure control function, described in [36], the depressurization of BZ/FW systems can be accomplished by manually triggering the pilot-operated relief valve (PORV). The pressure target value at the end of the depressurization phase was preliminarily set to 10 MPa, nearly keeping the same subcooling margin characterizing the PHTS in operating conditions [35].
- Gas temperature has been postulated as equal to the water temperature, T_{gas} = 295 °C. The main reason is to keep the BB internals hot and prevent operation below the ductile/brittle transition temperature due to neutron radiation. In the future, this parameter could be optimized accounting for the power needed to heat the gas up to such a temperature level.
- Water must be driven to a system hosting a storage volume large enough to accommodate all the PHTS inventory. The DEMO WCLL chemical volume control system (CVCS) has been preliminarily identified as the receiving system. Given the large water inventory to be drained (195.3 m^3, for both IB and OB), a storage system must be designed and integrated within the CVCS. The corresponding letdown path is connected to the cold leg piping of the BB PHTS, downstream the main circulation pumps, and will be used for the water/gas mixture discharging. Consequently, the gas injection pipeline must be connected to the hot section of the PHTS (e.g., on the sector outlet feeding pipes). To minimize CVCS requirements, we assume that the maximum draining flow is equal to the nominal letdown flow, 0.5% of nominal PHTS flow.

It should be noted that in the present design iteration, no DEMO subsystem exists to supply the high-temperature/high-pressure nitrogen at the required flow rate for BB draining.

Once the main assumptions were defined, two different models of the BZ circuit within DEMO WCLL COB segment were developed using RELAP5/Mod3.3 system thermal–hydraulic (STH) code [37] and OpenFOAM (OF) CFD code [38].

3.2.2. Numerical Models

The BZ cooling system geometry and STH nodalization scheme are illustrated in Figure 28. In the following, a synthetic description of both models is provided.

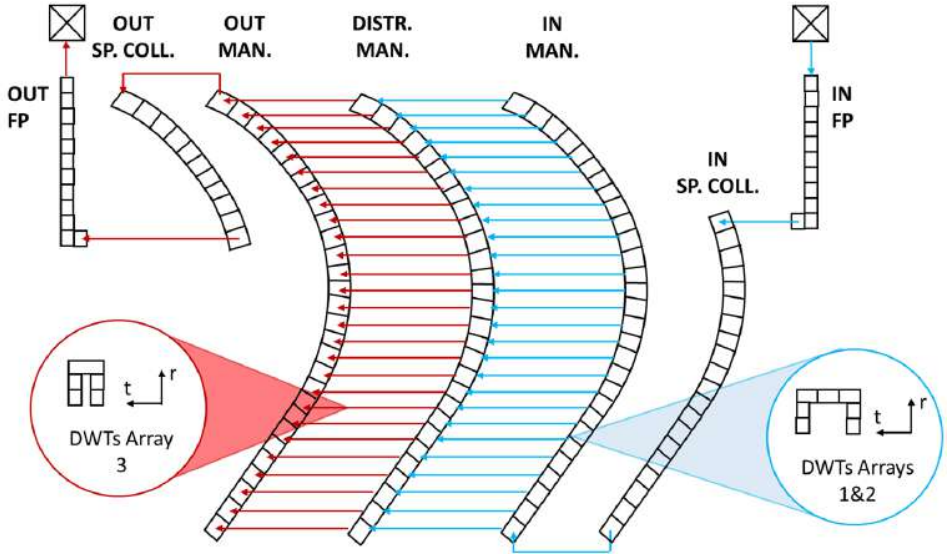

Figure 28. RELAP5/Mod3.3 nodalization of BZ circuit within DEMO WCLL COB segment.

Referring to the RELAP5/Mod3.3 input deck, the *slice nodalization technique* was adopted. A vertical discretization of the overall blanket segment was performed based on selected quotes. They were chosen considering the breeding cell elevations. The axial mesh related to all the COB components (feeding pipes, manifolds, sector collector, DWTs) was obtained respecting these reference fixed heights. As a result, the same mesh length (or submultiple) was used for the vertical control volumes belonging to different nodalization regions positioned at the same axial level. This technique improves the code modeling capabilities. When adopted, fluid properties are evaluated at the same axial elevations for all the nodalization regions, avoiding an error source in the simulation outcomes. Dedicated pipe components were used to model each element along the fluid flow path: the inlet feeding pipe, the spinal collector inlet section, the inlet/recirculation/outlet manifolds, the spinal collector outlet section and the outlet feeding pipe. For what concerns DWTs, they were simulated by using equivalent components. The tubes belonging to each breeding cell were collapsed into two pipes, one representing arrays 1 and 2 and one modeling array 3 (see Figure 28). Such components are characterized by lumped parameters (flow area and mass flow) to keep the correct hydraulic behavior. In the transient calculations, water and gas initial thermodynamic conditions (pressure and temperature) and gas-injected flow were all imposed as boundary conditions, according to the assumptions discussed above. The gas inlet mass flow was calculated to compensate for the reference water volume flow rate evacuated from the blanket (limited by the CVCS operational requirements).

CFD simulations were performed using the volume of fluid (VoF) interFoam multiphase solver available in the OF-9 distribution [38]. The water/nitrogen multiphase flow was assumed to be incompressible, immiscible and isothermal at the specified conditions. Problem geometry has been defined consistently with Figure 28. To reduce computational cost, hydraulic connections between parallel channels in spinal collectors and distribution manifolds were collapsed in fewer elements of the total equivalent cross-section as well as DWTs which have been grouped in 10 sections, split following the same array hierarchy represented in Figure 28, for which representative inclination, volume and radial length have been maintained. A symmetry boundary condition is imposed on the radial–poloidal midplane. A computational grid composed by unstructured tetrahedral elements for manifold and collectors and mapped hexahedral elements for DWTs was used. A typical mesh

is shown in Figure 29. Mesh sensitivity analysis was performed on prototypical geometries, while grid-independent results were achieved with a resolution equal to an element count of 550×10^3. Transient simulations were performed using second-order time and spatial discretization schemes. At t = 0, the system was supposed to be filled with water and at rest. At the inlet, a pure nitrogen volumetric flow rate was imposed, whereas a null total pressure was enforced at the outlet. No-slip and null pressure gradient boundary conditions were imposed on fluid/solid interfaces.

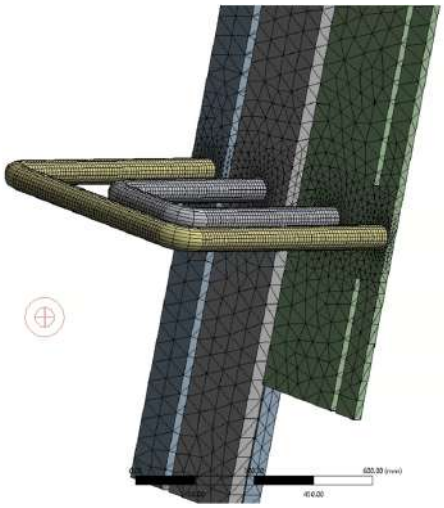

Figure 29. Detail of OpenF mesh close to the bottom end of COB segment. One of the DWT groups is shown: DWT arrays 1 and 2 (in yellow) connect inlet and distribution manifold; DWT array 3 (in grey) conveys water from distribution to outlet manifold.

3.2.3. Results and Discussion

The two models described were used to perform numerical simulations of the draining transient involving the COB segment. The main outcomes are collected in Table 5, Figures 30 and 31. The liquid void fraction (α_f) was selected as a reference figure of merit to discuss the simulation results. It clearly indicates the amount of segment volume still filled with liquid water at the end of the transient (EoT). Looking at Table 5, what can be observed is that there is accordance between the final liquid void fractions predicted at EoT by both models. Most of the remaining water is located in the DWTs and the inlet/outlet sections of the spinal collector (see Figures 30a and 31 referring to STH and CFD results, respectively). The former is due to the downward orientation of the components belonging to the breeding units situated in the upper part of the segment (above the equatorial plane). The poloidal profile of the residual liquid void fraction within DWTs at EoT is shown in Figure 30b, referring to the STH code. The correspondent distribution for CFD code can be seen in Figure 31. It should be noted that even if the CFD model features a reduced breeding unit number (only 10 DWT groups instead of 106), no significant loss of information is expected since the poloidal positions selected to be simulated are equally spaced along the poloidal coordinate and representative of the DWT vertical orientations. The distributions reported in Figures 30b and 31 are in accordance. Regarding the inlet/outlet sections of the spinal collector, the high liquid void fraction still present at EoT is due to its upward orientation. It must be recalled that, due to the gas injection/water draining chosen points, the fluid flow path within the COB segment during draining is reverted with respect to normal operations. Thus, inlet/outlet sections of the spinal collector are travelled upwards by a water/gas mixture, while inlet, outlet and distribution manifolds are travelled downwards. Thus, the draining of the latter is helped by gravity while the flush of the former is hampered.

Table 5. DEMO WCLL COB segment draining calculation results.

Residual Liquid Void Fraction ($\alpha_{f,i}$)	STH	CFD
DWTs ($\alpha_{f,DWT}$)	**0.31**	**0.39**
Inlet Spinal Collector	0.83	-
Inlet Manifold	0.01	-
Distribution Manifold	0.01	-
Outlet Manifold	0.01	-
Outlet Spinal Collector	0.47	-
Total Manifold ($\alpha_{f,M}$)	**0.21**	**0.29**
Total COB Segment (α_f)	**0.21**	**0.29**

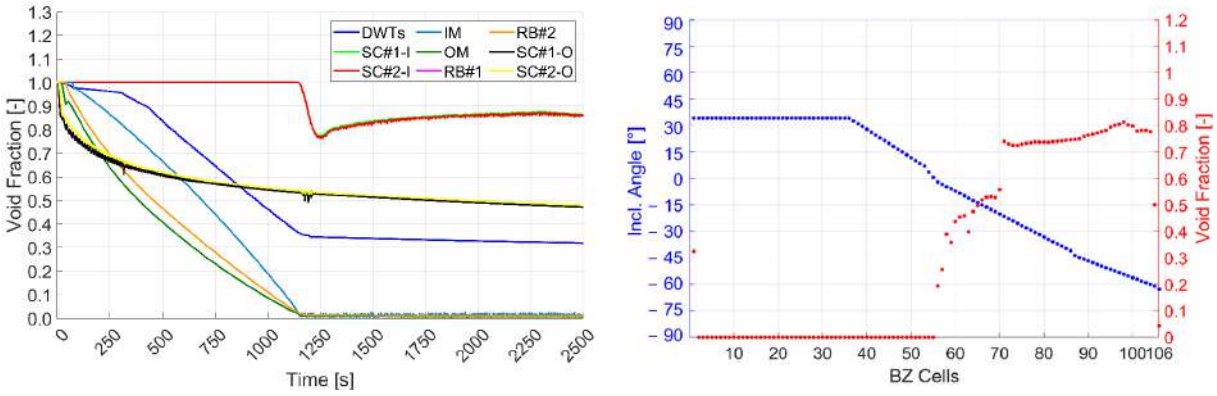

Figure 30. DEMO WCLL COB segment draining, RELAP5/Mod3.3 results: transient of the liquid void fraction within main segment components (**a**); distribution of the liquid void fraction within breeding units at the end of transient (**b**).

Figure 31. DEMO WCLL COB segment draining, OpenFOAM results: an overview of the liquid void fraction transient within the component.

The last important simulation result is the residual fluid mass present in BZ COB segment cooling system at EoT. It can be calculated as $m_{BZ} = \rho_f \alpha_f V_{BZ} + \rho_g \left(1 - \alpha_f\right) V_{BZ}$, with $V_{BZ} = 2.2652\ \mathrm{m}^3$, $\rho_f = 726.3\ \mathrm{kg/m}^3$, and $\rho_g = 59.3\ \mathrm{kg/m}^3$. It follows that $m_{BZ} = 451.6$ kg and $m_{BZ} = 623.6$ kg for STH and CFD, respectively. This parameter is the dominant contribution of the cooling system to the blanket sector dead weight, whose maximum value is a strict requirement coming from the remote handling system of the DEMO reactor. If necessary, m_{BZ} can be reduced by either allowing a higher draining flow rate at the CVCS (which will

improve the gas lift performances and prevent coolant stagnation in the spinal collectors) or, if this is not possible, by promoting evaporation through further coolant depressurization.

4. Conclusions

The conceptual design phase of DEMO started in 2021 under the umbrella of EUROfusion and Horizon Europe activities. The WCLL BB layout achieved at the end of the PCD phase is being modified to improve the BB performances and solve the existing issues.

To this end, the WCLL BB low TBR and reliability issues should benefit from the new proposed DWT layout. Indeed, some additional advantages with respect to the former C-shaped design should be underlined. First, the adoption of helical tubes implies a significant simplification of the BB layout. Indeed, it is easier to be manufactured/assembled, since DWTs can be inserted after the structural components (stiffening plates) are placed. Abandoning water recirculation allows an easier design of the water manifolds. Moreover, the lower total number of tubes, and consequently of welds against the in-vessel LOCA, should increase the reliability of the system. A total water volume reduction of 8.1% was calculated in the BZ with respect to the 24-tube configuration. This might help to increase the TBR. The manufacturability of DWTs with this configuration is being studied.

An effort was made to integrate the WCLL BB layout with the different in-vessel systems. Connecting pipes with BB coolant PHTS and TER loops have been successfully integrated within the design.

The design of a WCLL COB segment housing the cut-outs required by the ECH system is currently ongoing. Preliminary thermo-mechanical analyses have shown that the "modularity" of the current design allows integrating this system without a significant degradation of its structural performances, at least under the assessed scenarios. Further assessment accounting for EM loads will be performed.

Finally, dedicated simulations to analyze the draining of cooling water of the COB BZ circuit was carried out adopting different methods. The results highlighted that a fraction between 20% and 30% of the BZ water remains in the segment. The behavior of the COB FW cooling system and of IB segments may be evaluated in the future if deemed necessary to improve the accuracy of the BB dead weight estimate. The developed calculation methodology is currently being applied to the calculation of the residual mass fraction after the COB PbLi draining procedure.

Author Contributions: Conceptualization, P.A. and A.D.N.; software, I.C., C.C., A.C., M.D.O, V.I., P.M., L.M., S.N. and S.S.; writing—original draft preparation, P.A., G.B., P.A.D.M., F.G., F.M., R.M., L.S., A.T. and M.U.; writing—review and editing, P.A., A.D.N. and M.U.; supervision, A.D.N. and M.U. All authors have read and agreed to the published version of the manuscript.

Funding: This research was funded by the European Union via the Euratom Research and Training Programme, grant agreement no. 101052200—EUROfusion.

Acknowledgments: This work was carried out within the framework of the EUROfusion Consortium, funded by the European Union via the Euratom Research and Training Programme (grant agreement no. 101052200—EUROfusion). Views and opinions expressed are those of the authors only and do not necessarily reflect those of the European Union or the European Commission. Neither the European Union nor the European Commission can be held responsible for them.

Conflicts of Interest: The authors declare no conflict of interest.

Abbreviations

BB	breeding blanket
BC	bottom cell
BSS	back-supporting structure
BU	breeding unit
BZ	breeding zone
CC	central cell

CFD	computational fluid dynamics
COB	central outboard blanket
CVCS	chemical volume control system
DP	draining pipe
DWT	double-walled tubes
ECH	electron cyclotron heating
EM	electro-magnetic
EoT	end of the transient
EPP	equivalent porous pipe
FEM	finite element method
FP	feeding pipe
FW	first wall
GM	global model
HCPB	helium-cooled pebble bed
IB	inboard blanket
IM	inlet manifold
LOCA	loss of coolant accident
LTM	long term maintenance
MHD	magneto hydro-dynamic
NO	normal operation
OB	outboard blanket
OF	open foam
OM	outlet manifold
OP	over-pressurization
PCD	pre-conceptual design
PHTS	primary heat transfer system
PORV	pilot operated relief valve
RAFM	reduced activation ferritic martensitic
RANS	Reynolds-averaged Navier–Stokes (equations)
REC	recirculation manifold
RM	remote maintenance
SB	segment box
SM	sub-model
SP	stiffening plate
STH	system thermal–hydraulic
SW	side wall
TBM	test blanket module
TBR	tritium breeding ratio
TC	top cell
TER	tritium extraction and removal
TFC	toroidal field coil
UVDE	upper vertical displacement event
VV	vacuum vessel
WCLL	water-cooled lead lithium

References

1. Morris, W.; Litaudon, X.; Hidalgo, C.; McDonald, D.; Zohm, H.; Federici, G. *European Research Roadmap to the Realisation of Fusion Energy*; EUROFusion: Garching, Germany, 2018; ISBN 978-3-00-061152-0.
2. Boccaccini, L.V.; Arbeiter, F.; Arena, P.; Aubert, J.; Bühler, L.; Cristescu, I.; Del Nevo, A.; Eboli, M.; Forest, L.; Harrington, C.; et al. Status of Maturation of Critical Technologies and Systems Design: Breeding Blanket. *Fusion Eng. Des* **2022**, *179*, 113116. [CrossRef]
3. Arena, P.; Del Nevo, A.; Moro, F.; Noce, S.; Mozzillo, R.; Imbriani, V.; Giannetti, F.; Edemetti, F.; Froio, A.; Savoldi, L.; et al. The DEMO Water-Cooled Lead–Lithium Breeding Blanket: Design Status at the End of the Pre-Conceptual Design Phase. *Appl. Sci.* **2021**, *11*, 11592. [CrossRef]
4. Del Nevo, A.; Arena, P.; Caruso, G.; Chiovaro, P.; Di Maio, P.; Eboli, M.; Edemetti, F.; Forgione, N.; Forte, R.; Froio, A.; et al. Recent progress in developing a feasible and integrated conceptual design of the WCLL BB in EUROfusion project. *Fusion Eng. Des.* **2019**, *146*, 1805–1809. [CrossRef]
5. Catanzaro, I.; Bongiovì, G.; Di Maio, P.A. Analysis of the Thermo-Mechanical Behaviour of the EU DEMO Water-Cooled Lithium Lead Central Outboard Blanket Segment under an Optimized Thermal Field. *Appl. Sci.* **2022**, *12*, 1356. [CrossRef]

6. Maviglia, F.; Bachmann, C.; Federici, G.; Franke, T.; Siccinio, M.; Albanese, R.; Ambrosino, R.; Arter, W.; Bonifetto, R.; Calabrò, G.; et al. Integrated design strategy for EU_DEMO first wall protection from plasma transients. *Fusion Eng. Des.* **2022**, *177*, 113067. [CrossRef]
7. Moro, F.; Arena, P.; Catanzaro, I.; Colangeli, A.; Del Nevo, A.; Flammini, D.; Fonnesu, N.; Forte, R.; Imbriani, V.; Mariano, G.; et al. Nuclear performances of the water-cooled lithium lead DEMO reactor: Neutronic analysis on a fully heterogeneous model. *Fusion Eng. Des.* **2021**, *168*, 112514. [CrossRef]
8. Edemetti, F.; Di Piazza, I.; Del Nevo, A.; Caruso, G. Thermal-hydraulic analysis of the DEMO WCLL elementary cell: BZ tubes layout optimization. *Fusion Eng. Des.* **2020**, *160*, 111956. [CrossRef]
9. Fischer, U.; Bachmann, C.; Bienkowska, B.; Catalan, J.; Drozdowicz, K.; Dworak, D.; Leichtle, D.; Lengar, I.; Jaboulay, J.-C.; Lu, L.; et al. Neutronic analyses and tools development efforts in the European DEMO programme. *Fusion Eng. Des.* **2014**, *89*, 1880–1884. [CrossRef]
10. Fischer, U.; Bachmann, C.; Catalan, J.; Eade, T.; Flammini, D.; Gilbert, M.; Jaboulay, J.-C.; Konobeev, A.; Leichtle, D.; Lu, L.; et al. Methodological approach for DEMO neutronics in the European PPPT programme: Tools, data and analyses. *Fusion Eng. Des.* **2017**, *123*, 26–31. [CrossRef]
11. X-5 Monte Carlo Team. *MCNP—A General Monte Carlo N-Particle Transport Code*; Version 5; Los Alamos National Laboratory: Los Alamos, NM, USA, April 2003.
12. JEFF3.3 Nuclear Data Library. Available online: http://www.oecd-nea.org/dbdata/jeff/jeff33/#neutron (accessed on 16 February 2022).
13. Bachmann, C.; Ciattaglia, S.; Cismondi, F.; Eade, T.; Federici, G.; Fischer, U.; Franke, T.; Gliss, C.; Hernandez, F.; Keep, J.; et al. Overview over DEMO design integration challenges and their impact on component design concepts. *Fusion Eng. Des.* **2018**, *136*, 87–95. [CrossRef]
14. Available online: www.spaceclaim.com (accessed on 8 January 2023).
15. Wu, Y.; FDS Team. CAD-based interface programs for fusion neutron transport simulation. *Fusion Eng. Des.* **2009**, *84*, 1987–1992. [CrossRef]
16. Fischer, U.; Boccaccini, L.; Cismondi, F.; Coleman, M.; Day, C.; Hörstensmeyer, Y.; Moro, F.; Pereslalvtsev, P. Required, Achievable and Target TBR for the European DEMO. *Fusion Eng. Des.* **2020**, *155*, 111553. [CrossRef]
17. Allio, A.; Arena, P.; Del Nevo, A.; Savoldi, S. Hybrid modelling for the manifolds and coolant flow distribution in the Water-Cooled Lead-Lithium of the EU-DEMO reactor. In Proceedings of the 19th International Topical Meeting on Nuclear Reactor Thermal Hydraulics (NURETH-19), Brussels, Belgium, 6–11 March 2022.
18. Catanzaro, I.; Arena, P.; Del Nevo, A.; Di Maio, P.A.; Edemetti, F.; Forte, R.; Martelli, E. Parametric study of the influence of double-walled tubes layout on the DEMO WCLL breeding blanket thermal performances. *Fusion Eng. Des.* **2020**, *161*, 111893. [CrossRef]
19. Melchiorri, L.; Narcisi, V.; Giannetti, F.; Caruso, G.; Tassone, A. Development of a RELAP5/MOD3.3 module for MHD pressure drop analysis in liquid metals loops: Verification and Validation. *Energies* **2021**, *14*, 5538. [CrossRef]
20. Smolentsev, S. Physical background, computations and practical issues of the magnetohydrodynamic pressure drop in a fusion liquid metal blanket. *Fluids* **2021**, *6*, 110. [CrossRef]
21. Melchiorri, L.; Narcisi, V.; Ciurluini, C.; Giannetti, F.; Caruso, G.; Tassone, A. Preliminary MHD pressure drop analysis for the prototypical WCLL TBM with RELAP5/MOD3.3. *Fusion Eng. Des.* **2022**, *176*, 113048. [CrossRef]
22. Tassone, A.; Caruso, G.; Del Nevo, A. Influence of PbLi hydraulic path and integration layout on MHD pressure losses. *Fusion Eng. Des.* **2020**, *155*, 111517. [CrossRef]
23. Tassone, A.; Siriano, S.; Caruso, G.; Utili, M.; Del Nevo, A. MHD pressure drop estimate for the WCLL in-magnet PbLi loop. *Fusion Eng. Des.* **2020**, *160*, 111830. [CrossRef]
24. Sedlak, K.; Anvar, V.; Bagrets, N.; Biancolini, M.E.; Bonifetto, R.; Bonne, F.; Boso, D.P.; Brighenti, A.; Bruzzone, P.; Celentano, G.; et al. Advance in the conceptual design of the European DEMO magnet system. *Supercond. Sci. Technol.* **2020**, *33*, 044013. [CrossRef]
25. Martelli, D.; Venturini, A.; Utili, M. Literature review of lead-lithium thermophysical properties. *Fusion Eng. Des.* **2019**, *138*, 183–195. [CrossRef]
26. Bühler, L.; Mistrangelo, C. A simple MHD model for coupling poloidal manifolds to breeder units in liquid metal blankets. In Proceedings of the 32nd Symposium on Fusion Technology (SOFT), Dubrovnik, Croatia, 18–23 September 2022.
27. Siriano, S.; Tassone, A.; Melchiorri, L.; Caruso, G.; Arena, P. Numerical analysis of extreme magnetoconvective phenomena in the WCLL blanket. In Proceedings of the 32nd Symposium on Fusion Technology (SOFT), Dubrovnik, Croatia, 18–23 September 2022.
28. Yan, Y.; Alice, Y.; Abdou, M. Numerical study of magneto-convection flows in a complex prototypical liquid-metal fusion blanket geometry. *Fusion Eng. Des.* **2020**, *159*, 111688. [CrossRef]
29. Urgorri, F.R.; Fernández-Berceruelo, I.; Rapisarda, D. Magneto-Convective Analyses of the PbLi Flow for the EU-WCLL Fusion Breeding Blanket. *Energies* **2021**, *14*, 6192. [CrossRef]
30. Iannone, F.; Ambrosino, F.; Bracco, G.; De Rosa, M.; Funel, A.; Guarnieri, G.; Migliori, S.; Palombi, F.; Ponti, G.; Santomauro, G.; et al. CRESCO ENEA HPC clusters: A working example of a multifabric GPFS Spectrum Scale layout. In Proceedings of the 2019 International Conference on High Performance Computing & Simulation (HPCS), Dublin, Ireland, 15–19 July 2019; pp. 1051–1052.
31. Catanzaro, I.; Bongiovì, G.; Chiovaro, P.; Di Maio, P.A.; Spagnuolo, G.A. Development and application of an alternative modelling approach for the thermo-mechanical analysis of a DEMO Water-Cooled Lithium Lead Breeding Blanket Segment. *Fusion Eng. Des.* **2022**, *180*, 113195. [CrossRef]
32. AFCEN. *RCC-MRx, Design and Construction Rules for Mechanical Components of Nuclear Installations*; AFCEN: Courbevoie, France, 2013.
33. Tran, M.Q.; Agostinetti, P.; Aiello, G.; Avramidis, K.; Baiocchi, B.; Barbisan, M.; Bobkov, V.; Briefi, S.; Bruschi, A.; Chavan, R.; et al. Status and future development of Heating and Current Drive for the EU DEMO. *Fusion Eng. Des.* **2022**, *180*, 113159. [CrossRef]

34. Pinna, T.; Dongiovanni, D.N. Approach in improving reliability of DEMO. *Fusion Eng. Des.* **2020**, *161*, 111937. [CrossRef]
35. Barucca, L.; Hering, W.; Martin, S.P.; Bubelis, E.; Del Nevo, A.; Di Prinzio, M.; Caramello, M.; D'Alessandro, A.; Tarallo, A.; Vallone, E.; et al. Maturation of critical technologies for the DEMO balance of plant systems. *Fusion Eng. Des.* **2022**, *179*, 113096. [CrossRef]
36. Ciurluini, C.; Giannetti, F.; Del Nevo, A.; Caruso, G. Study of the EU-DEMO WCLL Breeding Blanket Primary Cooling Circuits Thermal-Hydraulic Performances during Transients Belonging to LOFA Category. *Energies* **2021**, *14*, 1541. [CrossRef]
37. Idaho National Laboratory; The RELAP5-3D© Code Development Team. *RELAP5-3D© Code Manual: Code Structure, System Models, and Solution Methods*; Revision 4.3, INL-MIS-15-36723; Idaho National Laboratory: Idaho Falls, ID, USA, 2015; Volume I.
38. OpenFOAM Foundation. OpenFoam v. 9, C++ Source Guide. Available online: https://cpp.openfoam.org/v9/interFoam_8C_source.html (accessed on 24 June 2022).